applied nano

MDPI

Article

Facile Synthesis of (Mn, Ce)Co-Doped ZnS Nanocrystals for Efficient Photocatalytic Degradation of Tetracycline

Pijush Das and Manos P. C. Kalita *

Department of Physics, Gauhati University, Guwahati 781014, India; pijush@gauhati.ac.in
* Correspondence: mpckalita@gauhati.ac.in

Abstract

Tetracycline contamination of water poses a serious threat to human health and aquatic ecosystems, highlighting the need for remediation. This study investigates the potential of co-doping ZnS nanocrystals with Mn and Ce to enhance their photocatalytic performance for tetracycline removal by altering defect-related trap states and localized charge distribution, with the material synthesis being carried out using the facile chemical co-precipitation method. Pure, 2% Mn-doped, and (Mn, Ce)co-doped [(2% Mn, 1% Ce) and (2% Mn, 2% Ce)] ZnS nanocrystals were synthesized, followed by characterization via XRD, TEM, FE-SEM, EDX, XPS, FT-IR, UV–visible spectroscopy, and PL spectroscopy. Both Mn doping and (Mn, Ce) co-doping decreased crystallite size while increasing lattice strain and dislocation density. The band gaps fall in the 3.20–3.30 eV range. The Mn-doped and (Mn, Ce)co-doped ZnS exhibited a yellow–orange PL. The pure, 2% Mn-doped, (2% Mn, 1% Ce)co-doped, and (2% Mn, 2% Ce)co-doped ZnS nanocrystals degraded 45%, 64%, 89%, and 92% tetracycline after 300 min of simulated sunlight irradiation, respectively, with the (2% Mn, 2% Ce)co-doped ZnS nanocrystals degrading 85% tetracycline after 180 min. The (Mn, Ce)co-doped ZnS nanocrystals are cost-effective, efficient, and recyclable photocatalysts for the remediation of tetracycline pollutants.

Keywords: ZnS; semiconductor nanocrystals; Mn, Ce; co-doping; structural properties; optical properties; Williamson–Hall; tetracycline; antibiotic; photocatalysis

1. Introduction

Antibiotics (e.g., tetracycline, ciprofloxacin, levofloxacin, and amoxicillin) are widely used to combat bacterial infections across healthcare, veterinary practices, and agriculture. However, residues of antibiotics discharged into water bodies through patient excretion, hospital wastewater, livestock farm drainage, and agricultural runoff have been a cause for concern in recent years [1,2]. This poses a serious threat to aquatic life and also fosters the development of antibiotic-resistant bacteria [2]. At the same time, antibiotic residues may enter the food chain, posing a serious risk to human health. To mitigate this, different methods are being adopted, viz. membrane filtration (offers physical separation) [3], biodegradation (utilizes specialized microbes to break down chemical structures) [4], adsorption (uses porous materials to trap molecules) [5], and semiconductor photocatalysis (uses light of energy equal to or greater than its band gap to produce reactive superoxide and hydroxyl radicals, which mineralize antibiotic residues into harmless byproducts) [5,6]. Because of its high efficiency and operational simplicity, photocatalysis has emerged as a leading technology for removing antibiotic pollutants from water [7]. Within this field,

Check for updates

Academic Editor: Christian Julien

Received: 7 September 2026
Revised: 3 November 2026
Accepted: 4 November 2026
Published: 10 November 2026

Copyright: © 2026 by the authors. Licensee MDPI, Basel, Switzerland. This article is an open access article distributed under the terms and conditions of the Creative Commons Attribution (CC BY) license.

semiconductor nanomaterials have attracted intense research interest as advanced photocatalysts. With a higher surface area-to-volume ratio than their bulk counterparts, these nanomaterials provide abundant active sites, enhance reaction kinetics, and enable efficient removal of antibiotic pollutants from water [8].

ZnS is a prominent II-VI semiconductor known for its versatile physicochemical properties and widespread applications. It is one of the earliest identified semiconductors, which exists in two different crystal structures, viz., cubic zinc blende and hexagonal wurtzite [9,10]. With the emergence of nanoscience and nanotechnology, research focus has progressed from bulk ZnS to its nanostructured forms. These nanostructures often exhibit altered physical and chemical properties from their bulk counterparts, offering unique opportunities to investigate and fine-tune their structural, optical, magnetic, and photocatalytic properties. Researchers have employed various synthetic strategies to produce nanostructured ZnS, including chemical co-precipitation [11], hydrothermal [12], solvothermal [13], sol–gel [14], spray pyrolysis [15], and ball milling [16]. Furthermore, the literature reports the synthesis of various ZnS morphologies, such as nanospheres [17], nanorods [18], nanoflowers [19], and nanosheets [20]. These diverse aspects enable ZnS nanostructures to excel in different fields, including photocatalysis [21], spintronics [22], antimicrobial medicines [23], energy storage [24], and photovoltaics [25]. In recent years, the synergistic effects of co-doping in ZnS matrices have attracted significant research interest. Co-doped ZnS systems such as (Co, Cu) [26], (Cu, Bi) [27], (Mn, Cr) [11], (Cu, Mg) [28], (Cu, Mn) [28], (Cu, Ag) [28], (Cu, Fe) [29], and (Mn, Co) [30] have demonstrated high efficiency in the photocatalytic degradation of organic dyes. The functional versatility of co-doped ZnS has been observed in many other fields, such as Er-Yb co-doping for anti-counterfeiting [31], (N, S) co-doping for electrocatalysts in rechargeable zinc-air batteries [32], (Cu, Fe) co-doping for antibacterial activity [29], and (Co, Cu) co-doping for enhanced ferromagnetism [26].

Although various doped ZnS systems have recently been studied regarding the photodegradation of antibiotics [33–39], the efficacy of co-doped ZnS in this specific application remains largely unexplored. Since Ce ions possess a larger ionic radius (Ce^{3+}/Ce^{4+} ionic radius is 1.03 Å/0.93 Å) [40] than Mn^{2+} (0.83 Å) [41], their incorporation into the ZnS lattice, in addition to Mn^{2+} ions, can induce structural distortion, which may facilitate alterations in the microstructure, electronic band structure, etc., and thereby affect their various properties. Previous research on (Mn, Ce)co-doped ZnS is limited [42,43]. Sakthivel et al. [42] reported on the structural, optical, and electrochemical properties of (Mn, Ce)co-doped ZnS nanocrystals prepared by the co-precipitation method. Yang et al. [43] reported on the luminescence properties of (Mn, Ce)co-doped ZnS phosphors prepared by the solid-state sintering method. From an environmental viewpoint, tetracycline, a widely used antibiotic in both healthcare and livestock farming, is one of the most frequently detected antibiotic pollutants in water [44,45]. The application of doped ZnS nanocrystals for the photocatalytic degradation of tetracycline remains limited [37–39]. Li et al. [37] reported on hydrothermal synthesis of Cu-doped ZnS nanocrystals and their application in tetracycline degradation under visible light. Das et al. [38] recently reported on protein-assisted synthesis of Mn-doped ZnS nanocrystals for photocatalytic tetracycline degradation. Ibrahim et al. [39] reported on solvothermal synthesis of Cd-doped ZnS nanocrystals for efficient removal of tetracycline from aqueous solution through visible-light photocatalysis. The present study investigates the properties of pure, 2% Mn-doped, and (Mn, Ce)co-doped [(2% Mn, 1% Ce) and (2% Mn, 2% Ce)] ZnS nanocrystals synthesized via a cost-effective chemical co-precipitation route. The efficacy of the synthesized materials for the photocatalytic degradation of tetracycline antibiotics under simulated sunlight has been evaluated. Prepared by

a straightforward, cost-effective method, these materials, especially the (Mn, Ce)co-doped ones, are considerably efficient for the photodegradation of tetracycline antibiotics.

2. Photocatalytic Set-Up

The photocatalytic activities of the pure, 2% Mn-doped, and (Mn, Ce)co-doped [(2% Mn, 1% Ce) and (2% Mn, 2% Ce)] ZnS nanocrystals have been evaluated using tetracycline as an antibiotic pollutant. Figure 1 illustrates the setup used for the photocatalysis experiments. The components included a wooden box, a light source, an exhaust fan, a double-walled beaker with a water-circulation facility, and a magnetic stirrer. The wooden box was fitted with a solar simulator lamp (Osram Ultra-Vitalux, 300 W, Augsburg, Germany).

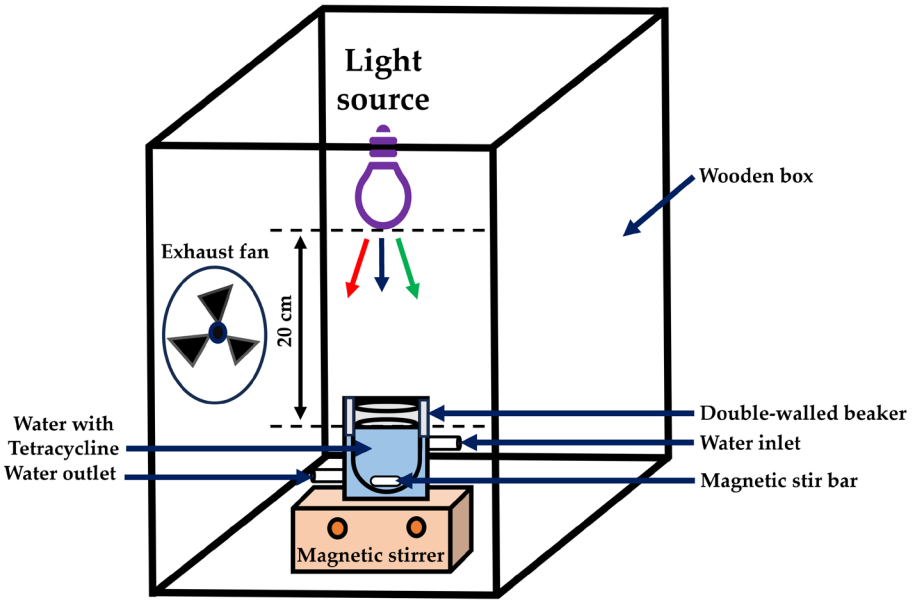


Figure 1. Schematic representation of the photocatalytic setup.

3. Models Used for XRD Line Profile Analysis

The average crystallite size, lattice strain, and dislocation density of the nanocrystals have been calculated through a comprehensive XRD line profile analysis. The width of an XRD line profile is influenced by these factors, as well as by instrumental-related factors. Therefore, it is imperative to remove the contribution of instrumental factors to the width of an XRD line profile to obtain material-related information. The instrumental-corrected FWHM, β of an XRD line profile, is obtained using the equation [46],

$$\beta = \beta_{exp} - \beta_{inst} \quad (1)$$

where β_{exp} is the FWHM extracted from an XRD line of the material, and β_{inst} is the FWHM extracted from an XRD pattern of a reference material that is well-crystallized. In the present case, the standard Si sample has been used as the reference material.

The average crystallite size and lattice strain of the synthesized materials have been calculated using the WH method represented by the equation [47,48],

$$\Delta K = \frac{0.9}{D} + 2\varepsilon K \quad (2)$$

where $\Delta K = \frac{\beta \cos\theta}{\lambda}$, $K = \frac{2 \sin\theta}{\lambda}$, D is crystallite size, ε is lattice strain, and λ is the wavelength of the X-rays used (0.15406 nm).

The WH method assumes that lattice strain uniformly influences XRD peak broadening across different crystallographic directions and therefore does not account for the anisotropic nature of peak broadening. Ungar et al. [49] have modified the WH model to incorporate the anisotropic XRD peak broadening due to lattice strain. They considered that edge and screw dislocations contribute to lattice strain and introduced dislocation contrast factors for different crystallographic planes into the WH equation. This new approach to XRD line profile analysis is known as the MWH method. The related equation is given by [49],

$$\Delta K = \frac{0.9}{D} + \left(\frac{\pi b^2 \rho}{2B}\right)^{1/2} K C_{hkl}^{1/2} \quad (3)$$

where C_{hkl}, 'b', and ρ are the average dislocation contrast factor, the modulus of the Burgers vector of dislocations, and dislocation density, respectively. The value of 'B' is taken as 10 for a wide range of dislocations [50]. For a crystal with face-centered cubic structure, the value of 'b' is $a/\sqrt{2}$, where 'a' is the lattice parameter [51]. The values of dislocation contrast factors C_{111}, C_{200}, C_{220}, C_{311}, and C_{400} have been taken as 0.1088, 0.2607, 0.1467, 0.1891, and 0.2607, respectively [52].

4. Results and Discussion

4.1. Chemical Co-Precipitation Synthesis of Materials

The facile chemical co-precipitation method was employed to synthesize pure, 2% Mn-doped, and (Mn, Ce)co-doped [(2% Mn, 1% Ce) and (2% Mn, 2% Ce)] ZnS nanocrystals. The chemical co-precipitation method offers operational and economic advantages over high-pressure, energy-intensive techniques such as hydrothermal and solvothermal synthesis. It can be carried out under ambient conditions, typically at relatively low temperatures and atmospheric pressure, without the need for costly autoclaves, reducing overall energy consumption as well. Moreover, high chemical homogeneity (a very uniform atomic or molecular mixture), control over particle size and morphology, the ability to modify simple parameters—such as pH, temperature, stirring speed, and molar ratios—or to incorporate surfactants/additives, and scalability and high yield for industrial-scale production are other important aspects of the chemical co-precipitation method. The chemicals used for the synthesis of the materials were zinc (II) chloride ($ZnCl_2$, Merck, Merck Life Science Pvt. Ltd., Mumbai, India), sodium sulphide nonahydrate ($Na_2S{\cdot}9H_2O$, Merck KGaA, Darmstadt, Germany), manganese (II) chloride tetrahydrate ($MnCl_2{\cdot}4H_2O$, Merck KGaA, Darmstadt, Germany), and cerium (III) chloride heptahydrate ($CeCl_3{\cdot}7H_2O$, Merck KGaA, Darmstadt, Germany). To synthesize pure ZnS, 1 M solutions of zinc chloride and sodium sulphide were separately prepared in 20 mL of deionized water. The solutions were mixed at room temperature and left undisturbed for 48 h. In an earlier report, Mamiyev et al. [53] observed formation of ZnS nanocrystals of sizes 5.3 nm, 7.5 nm, and 9.7 nm for reaction times of 5 h, 5.5 h, and 6 h, respectively. In the present work, the reaction time was kept relatively long to allow ample time for particle growth. The resulting precipitates were filtered, washed using deionized water, and dried under ambient conditions for several hours. Finally, the precipitates were ground into powder for further characterization and application. For the synthesis of 2% Mn-doped ZnS nanocrystals, separate solutions of 0.98 M zinc chloride, 0.02 M manganese chloride, and 1 M sodium sulphide were prepared in 20 mL of deionized water each. The zinc chloride and manganese chloride solutions were mixed, which was followed by the addition of the sodium sulphide solution. The subsequent aging, filtration, drying, and grinding steps were identical to those used in the adopted process for pure ZnS. For the synthesis of (Mn, Ce)co-doped ZnS nanocrystals, solutions of (0.98-x) M zinc chloride, 0.02 M manganese chloride, x M cerium chloride, and 1 M sodium sulphide were separately prepared in 20 mL of deionized water. To synthesize ZnS nanocrystals co-doped

with 2% Mn and varying concentrations of Ce, viz. 1% and 2%, the corresponding x values were taken as 0.01 and 0.02. The zinc chloride, manganese chloride, and cerium chloride solutions were mixed, which was followed by the addition of the sodium sulphide solution. The final processing steps followed the procedure used to synthesize pure ZnS nanocrystals.

4.2. XRD Studies

The XRD patterns of the materials were recorded using a powder X-ray diffractometer (Empyrean, Malvern Panalytical, Almelo, The Netherlands with CuK_{α} radiation, $\lambda = 1.5406$ Å). The X-ray generator was operated at 40 kV and 30 mA. Figure 2 shows the XRD patterns of the pure, 2% Mn-doped, and (Mn, Ce)co-doped [(2% Mn, 1% Ce) and (2% Mn, 2% Ce)] ZnS nanocrystals in the 2θ (θ is Bragg's angle) range of 20° to 75°. For the pure ZnS material, the diffraction peaks located at 2θ values of 28.61°, 33.12°, 47.64°, 56.49°, 59.59°, and 69.67° align perfectly with the (111), (200), (220), (311), (222), and (400) planes of the cubic zinc blende phase (ICDD file no.: 00-005-0566) of ZnS. A defining feature of these profiles is their broadening, indicating small crystallite size and significant lattice strain. Upon introducing Mn and Ce dopants, the zinc blende structure of ZnS remains intact, as evidenced by the persistence of the (111), (200), (220), (311), and (400) reflections. However, the 2% Mn-doped ZnS nanocrystals and both the (Mn, Ce)co-doped ZnS show broader XRD line profiles than the pure material. The peak position corresponding to the (111) plane was used for the calculation of the lattice parameter using Bragg's law. The values are found to be 5.402 ± 0.002 Å, 5.410 ± 0.002 Å, 5.415 ± 0.002 Å, and 5.419 ± 0.002 Å for pure, 2% Mn-doped, (2% Mn, 1% Ce)co-doped, and (2% Mn, 2% Ce)co-doped ZnS nanocrystals, respectively. Thus, the lattice parameter is larger in the doped materials than in pure ZnS. This change in lattice parameter is attributed to the substitution of Zn^{2+} ions (ionic radius 0.74 Å) [54] with larger ions, viz. Mn^{2+} (0.83 Å) [41] in the case of Mn-doped ZnS, and Mn^{2+} and Ce^{4+} (0.93 Å) [40] in the case of (Mn, Ce)co-doped ZnS. Figure 3 shows the WH plots for the materials. The average crystallite sizes of the pure, 2% Mn-doped, (2% Mn, 1% Ce)co-doped, and (2% Mn, 2% Ce)co-doped ZnS nanocrystals obtained from these plots are 16 nm, 11 nm, 9 nm, and 9 nm, respectively, while the corresponding lattice strains are 4.5×10^{-3}, 5.8×10^{-3}, 6.8×10^{-3}, and 6.8×10^{-3}. The average crystallite sizes of the pure, 2% Mn-doped, (2% Mn, 1% Ce)co-doped, and (2% Mn, 2% Ce)co-doped ZnS nanocrystals obtained from the MWH plots illustrated in Figure 4 are 14 nm, 10 nm, 8 nm, and 8 nm, respectively, while the corresponding dislocation densities are 1.1×10^{16} m^{-2}, 1.8×10^{16} m^{-2}, 2.4×10^{16} m^{-2}, and 2.4×10^{16} m^{-2}. Crystallite size decreases with Mn incorporation into ZnS, with even lower values for the (Mn, Ce)co-doped materials. Dopant segregation at grain boundaries hinders crystal growth, which may explain the lower crystallite sizes observed in Mn-doped and (Mn, Ce)co-doped ZnS nanocrystals compared with the pure ones. Furthermore, lattice strain and dislocation densities increase with Mn doping and (Mn, Ce) co-doping in ZnS.

4.3. TEM, FE-SEM, and EDX Studies

The TEM (JEM-2100F, JEOL Ltd., Tokyo, Japan) operated at an accelerating voltage of 200 kV was used to obtain the microstructural information of the pure and (2% Mn, 2% Ce)co-doped ZnS nanocrystals. Figure 5a,b show the TEM micrographs of pure and (2% Mn, 2%Ce)-co-doped ZnS nanocrystals. These micrographs show crystallite agglomeration, a typical feature of polycrystalline materials. Figure 6a,b present the HR-TEM micrographs of the pure and (2% Mn, 2% Ce)co-doped ZnS nanocrystals, respectively. Figure 6a shows a 14 nm crystallite in pure ZnS nanocrystals, while Figure 6b shows an 8.2 nm crystallite in (2% Mn, 2% Ce)co-doped ZnS nanocrystals. Both crystallites have an interplanar spacing of 0.27 nm, showing they correspond to the ZnS (200) plane. The MWH

method yielded crystallite sizes of 14 nm and 8 nm for pure and (2% Mn, 2% Ce)co-doped ZnS nanocrystals, as discussed earlier; therefore, the measured sizes from the HR-TEM micrographs agree well with those calculated from the XRD line-profile analysis.

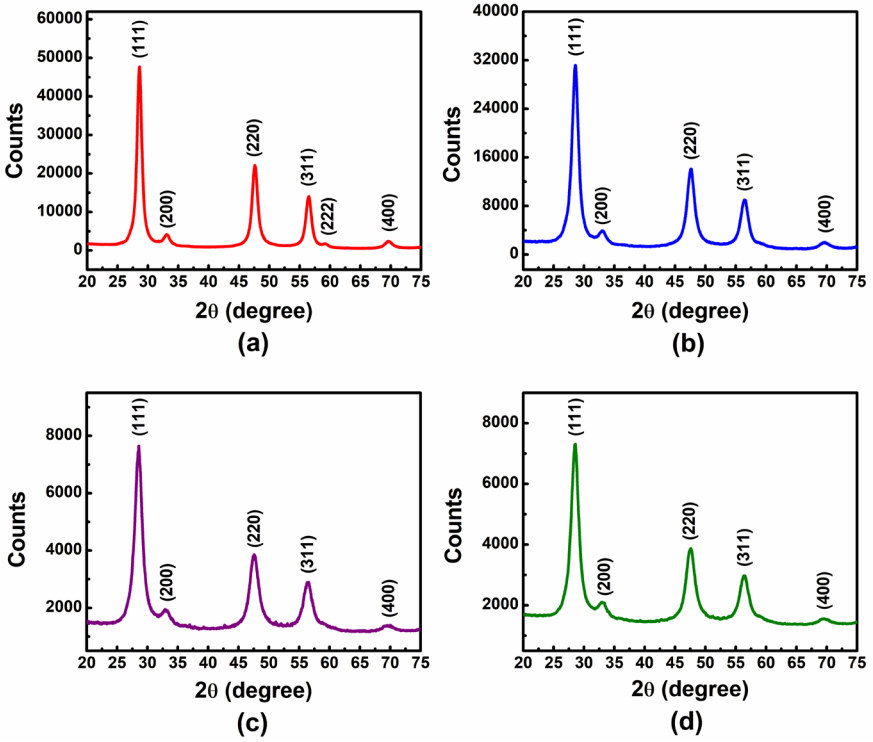


Figure 2. XRD patterns of (**a**) pure, (**b**) 2% Mn-doped, (**c**) (2% Mn, 1% Ce)co-doped, and (**d**) (2% Mn, 2% Ce)co-doped ZnS nanocrystals.

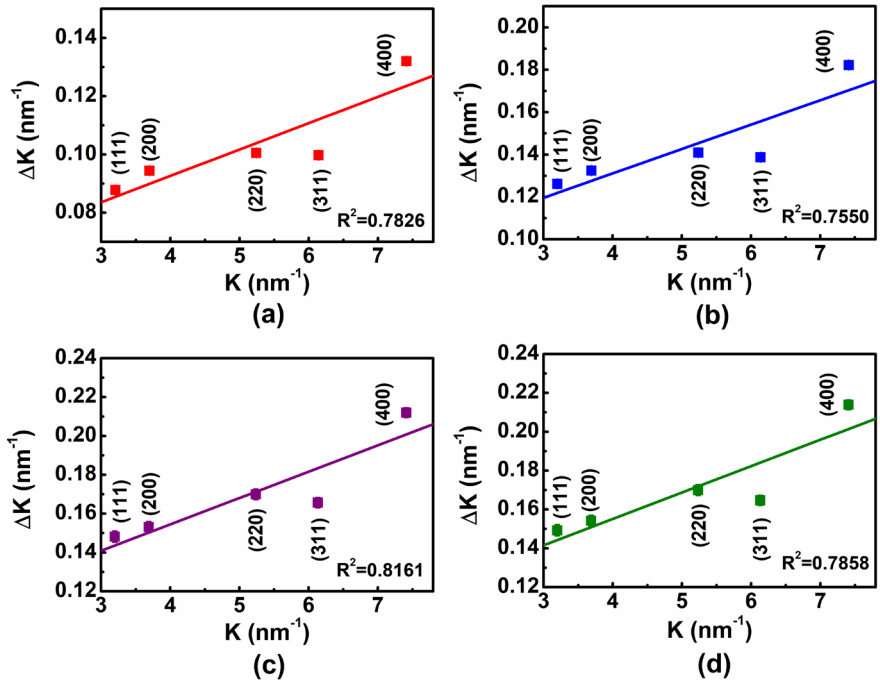


Figure 3. WH plots of (**a**) pure, (**b**) 2% Mn-doped, (**c**) (2% Mn, 1% Ce)co-doped, and (**d**) (2% Mn, 2% Ce)co-doped ZnS nanocrystals.

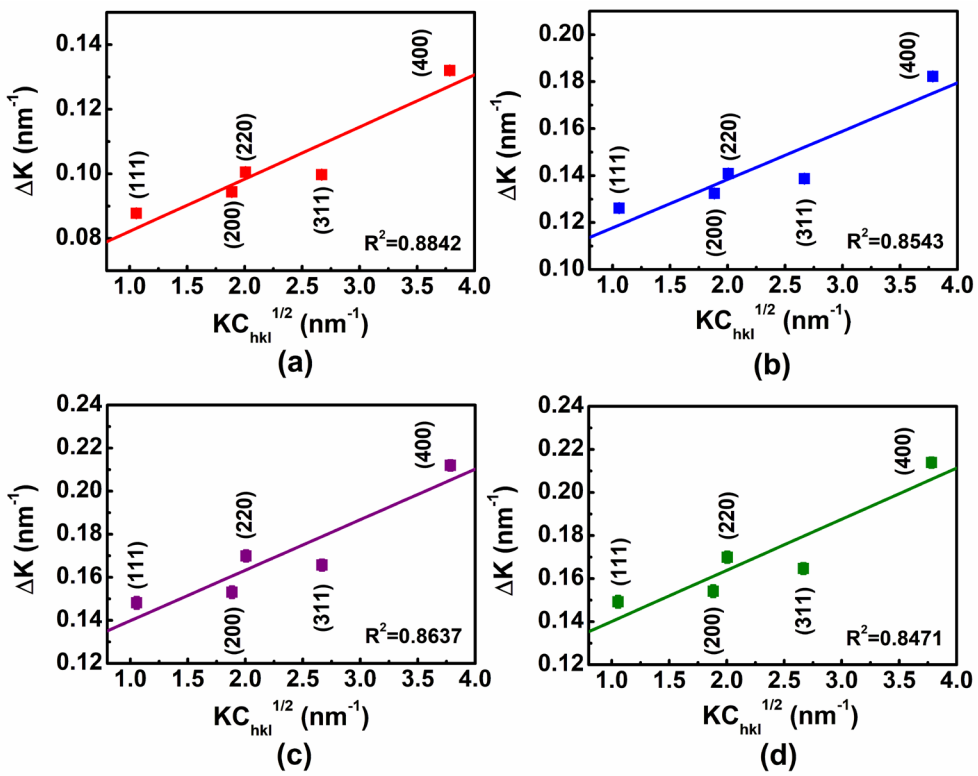


Figure 4. MWH plots of (**a**) pure, (**b**) 2% Mn-doped, (**c**) (2% Mn, 1% Ce)co-doped, and (**d**) (2% Mn, 2% Ce)co-doped ZnS nanocrystals.

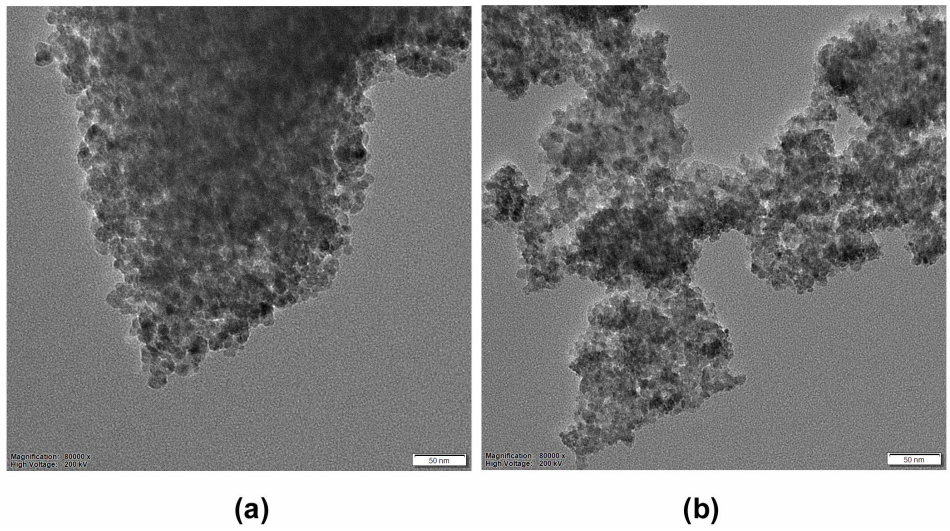


Figure 5. TEM micrographs of (**a**) pure and (**b**) (2% Mn, 2% Ce)co-doped ZnS nanocrystals.

The FE-SEM (Sigma 300, ZEISS, Jena, Germany) with an EDX spectrometer (EDAX, AMETEK Inc., Mahwah, NJ, USA) attachment was used to investigate surface morphology and elemental composition. Accelerating voltages of 5 kV and 15 kV were used to record the micrographs and EDX spectra of the materials, respectively. The FE-SEM micrograph of (2% Mn, 2% Ce)co-doped ZnS nanocrystals presented in Figure 7a shows an agglomerated particle morphology. The EDX spectrum and elemental maps for the (2% Mn, 2% Ce)co-doped ZnS nanocrystals, shown in Figures 7b and 7c, respectively, confirm the presence of the intended elements. The atomic percentages of Zn, S, Mn, and Ce in the (2% Mn, 2% Ce)co-doped ZnS nanocrystals are found to be 47.71%, 47.80%, 2.58%, and

1.91%, respectively, showing good agreement between the measured and targeted dopant concentrations.

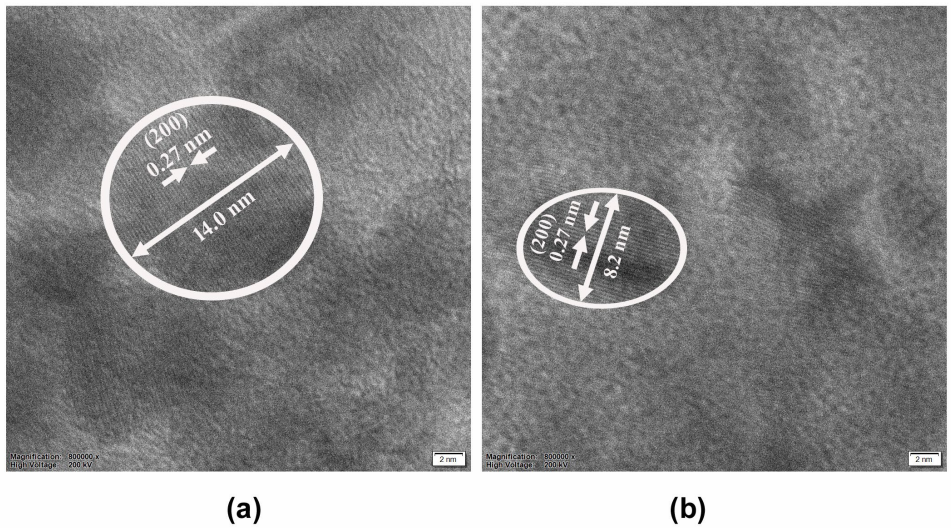


Figure 6. HR-TEM micrographs of (**a**) pure and (**b**) (2% Mn, 2% Ce)co-doped ZnS nanocrystals.

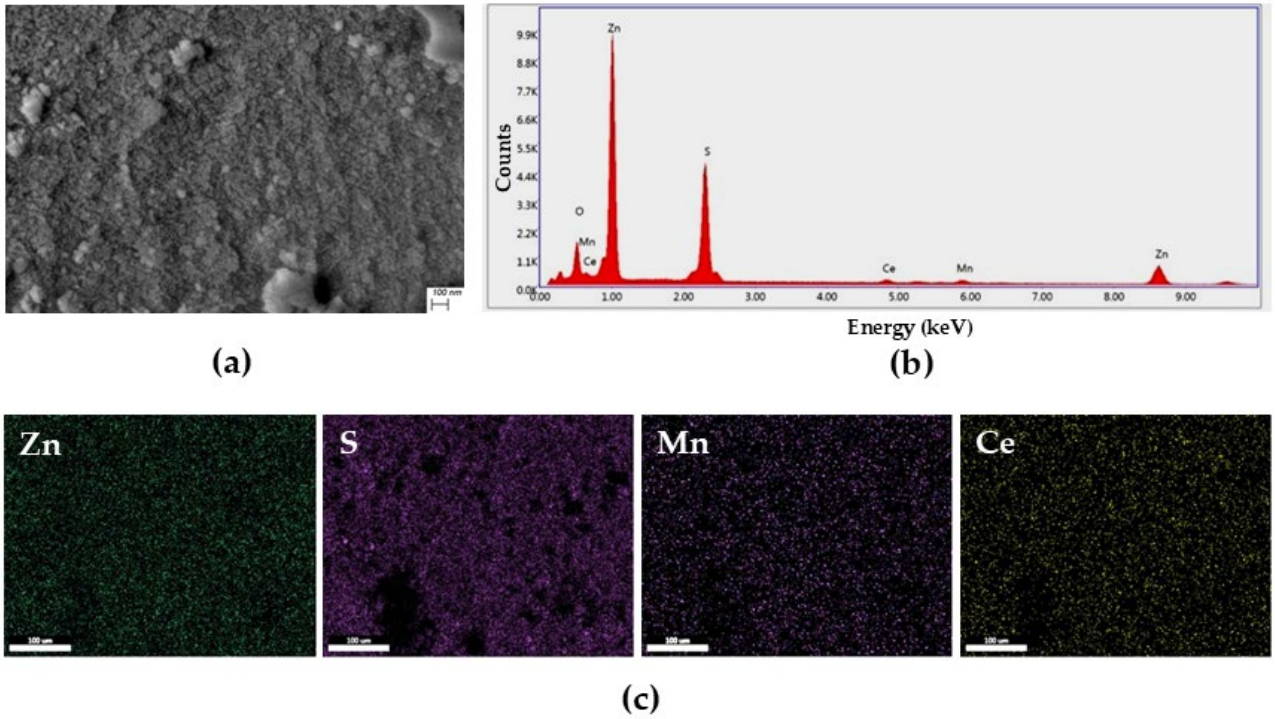


Figure 7. (**a**) FE-SEM micrograph, (**b**) EDX spectrum, and (**c**) elemental maps for different elements of (2% Mn, 2% Ce)co-doped ZnS nanocrystals.

4.4. FT-IR Studies

The FT-IR spectrometer equipped with an ATR facility (ALPHA, Bruker, Ettlingen, Germany; wavenumber range: 500–4000 cm^{-1}) was used to study chemical bonding in the materials. Figure 8 illustrates the FT-IR spectra of the pure, 2% Mn-doped, and (Mn, Ce)co-doped [(2% Mn, 1% Ce) and (2% Mn, 2% Ce)] ZnS nanocrystals. The bands at 3430 cm^{-1} and 1630 cm^{-1} correspond to O-H stretching and O-H bending vibrations, respectively [55]. The weak bands at 2930 cm^{-1} and 2850 cm^{-1} are attributed to the asymmetric and symmetric CH_2 stretching vibrations, respectively, which may arise from trace amounts of atmospheric hydrocarbons adsorbed on the material surface [56,57]. Two strongly infrared-active modes

are attributed to the fundamental vibrations of the sulphate group; they are observed at 1110 cm^{-1} (ν_3, antisymmetric S–O stretching) and 618 cm^{-1} (ν_4, antisymmetric angular deformation) [58–61]. The absorption at 618 cm^{-1} can be ascribed to the Zn-S bond vibration as well [62,63].

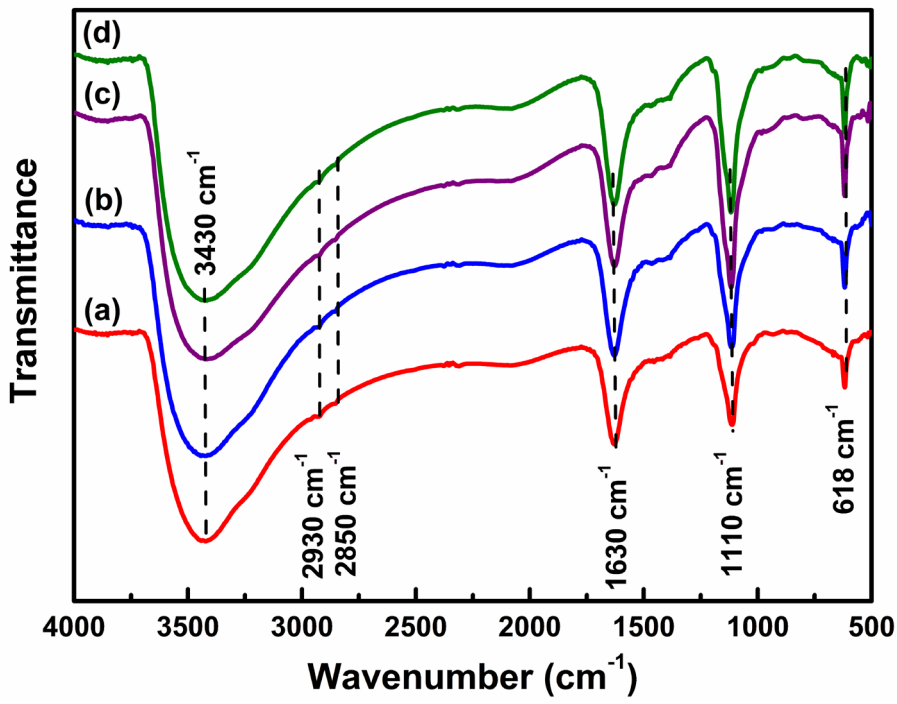


Figure 8. FT-IR spectra of (a) pure, (b) 2% Mn-doped, (c) (2% Mn, 1% Ce)co-doped, and (d) (2% Mn, 2% Ce)co-doped ZnS nanocrystals.

4.5. XPS Studies

The XPS measurements were carried out using AXIS Supra+, Kratos Analytical Ltd., Manchester, UK, XPS with a monochromatic X-ray source: AlK_α- 1486.6 eV. The binding energies were calibrated using the C 1 s peak at 284.8 eV as the reference. Figure 9 shows the XPS results for (2% Mn, 2% Ce)co-doped ZnS nanocrystals. Figure 9a shows peaks at 1045.4 eV and 1022.2 eV, corresponding to Zn $2p_{1/2}$ and Zn $2p_{3/2}$, respectively [64]. The peaks at 163.0 eV and 161.8 eV correspond to S $2p_{1/2}$ and S $2p_{3/2}$, respectively (Figure 9b) [64]. The high-resolution XPS spectrum of Mn $2p_{3/2}$ shows a peak at 640.9 eV (Figure 9c), indicating the presence of the Mn^{2+} state [65]. PL studies show a yellow–orange emission at 580 nm (discussed later in the article), which originates from Mn^{2+} [66]. Thus, the XPS and PL studies complement each other regarding the oxidation state of Mn in the (2% Mn, 2% Ce)co-doped ZnS nanocrystals. The Ce 3d spectrum of (2% Mn, 2% Ce)co-doped ZnS nanocrystals (Figure 9d) shows peaks at 916.9 eV, 908.1 eV, 901.1 eV, 898.7 eV, 886.6 eV, and 882.5 eV, corresponding to the Ce^{4+} state [67,68]. Thus, the XPS studies reveal the presence of Mn^{2+} and Ce^{4+} in the (2% Mn, 2% Ce)co-doped ZnS nanocrystals. Using $CeCl_3 \cdot 7H_2O$ as a Ce precursor in the synthesis of (Mn, Ce)co-doped material, the observation of Ce in the +4 oxidation state suggests that defect-mediated charge compensation maintains charge neutrality to accommodate the dopants. Notably, earlier studies have reported the appearance of the Ce^{4+} state in Ce-doped ZnS nanocrystals alongside the Ce^{3+} state, eVen though cerium (III) nitrate or cerium (III) acetate was used in synthesizing the materials [69,70].

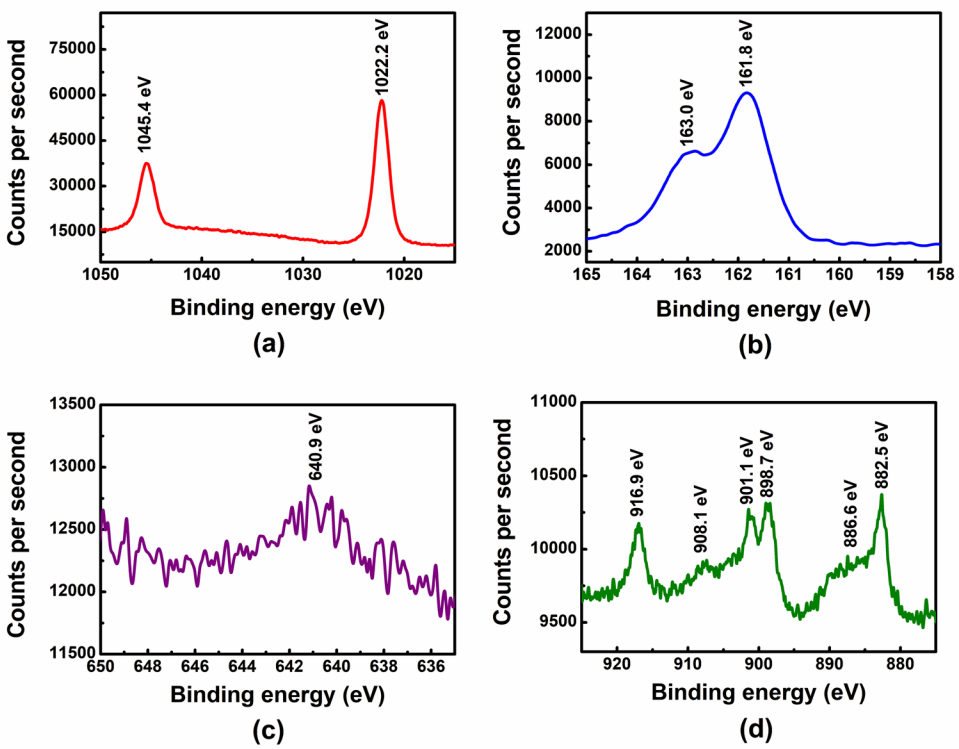


Figure 9. High-resolution XPS spectra for (**a**) Zn 2p, (**b**) S 2p, (**c**) Mn $2p_{3/2}$, and (**d**) Ce 3d for (2% Mn, 2% Ce)co-doped ZnS nanocrystals.

4.6. UV–Visible Absorption Studies

A double-beam UV–visible spectrophotometer (UV-1800, Shimadzu Corporation, Kyoto, Japan; wavelength range: 190–1100 nm) was used to record the absorption spectra of water-dispersed materials. Figure 10 depicts the UV–visible absorption spectra of the pure, 2% Mn-doped, and (Mn, Ce)co-doped [(2% Mn, 1% Ce) and (2% Mn, 2% Ce)] ZnS nanocrystals. The Tauc method was used to determine the band gaps of the nanocrystals from these spectra. Tauc's relation is given by [29,71],

$$(\alpha h\nu)^2 = K(h\nu - E_g) \quad (4)$$

where α, $h\nu$, and E_g are the absorption coefficient, photon energy, and band gap, respectively; while K is a constant. Figure 11 shows the Tauc plots for the various materials. The band gaps of the pure, 2% Mn-doped, (2% Mn, 1% Ce)co-doped, and (2% Mn, 2% Ce)co-doped ZnS nanocrystals are found to be 3.30 eV, 3.27 eV, 3.24 eV, and 3.20 eV, respectively. The band gap of the pure ZnS nanocrystals is lower than the bulk band gap of ZnS (3.67 eV) [72], which may be due to the presence of strains and defects. The observed band gap of 3.30 eV in pure ZnS agrees well with some earlier reports [27,72,73]. Khan et al. [27] reported on the observation of a band gap of 3.30 eV in ZnS nanocrystals prepared by a wet chemical route. Han et al. [72] reported on the observation of a band gap of 3.29 eV in ZnS nanoparticles prepared by a hot injection method. Yang et al. [73] reported on the exhibition of a band gap of 3.24 eV in ZnS nanocrystals prepared by a hydrothermal method. Furthermore, a reduction in the band gap after Mn-doping and (Mn, Ce) co-doping has been observed, which is attributed to the introduction of additional energy levels due to dopants. Such a reduction in band gaps has been observed previously for Cu-doped ZnS nanocrystals, as reported by Chandrika et al. [29].

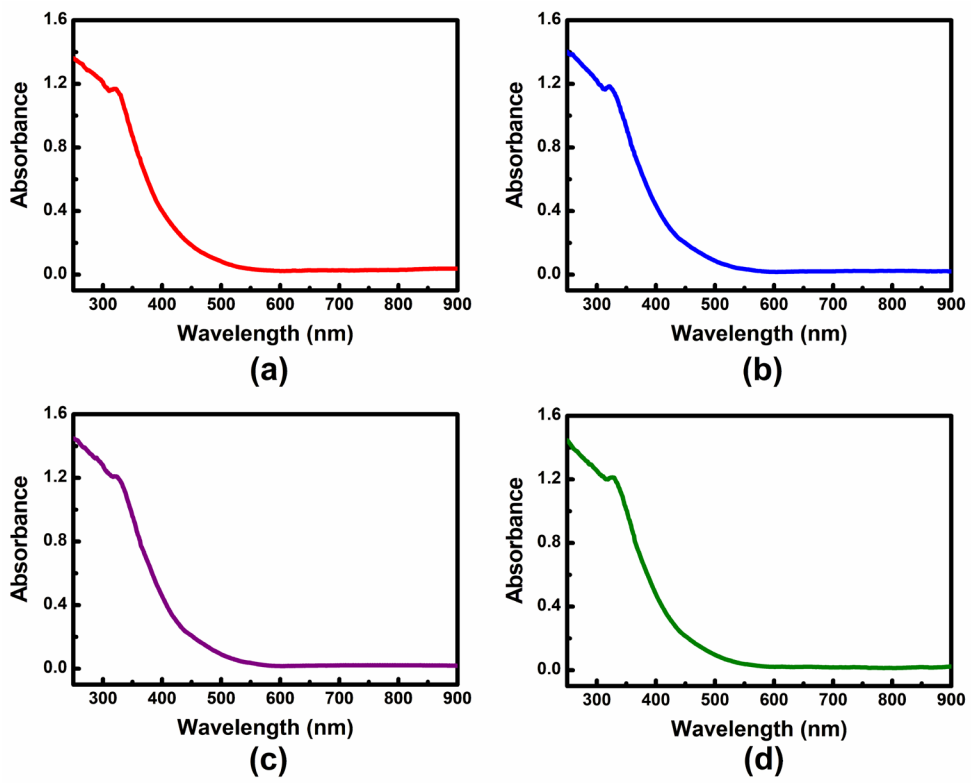


Figure 10. UV–visible absorption spectra of (**a**) pure, (**b**) 2% Mn-doped, (**c**) (2% Mn, 1% Ce)-co-doped, and (**d**) (2% Mn, 2% Ce)co-doped ZnS nanocrystals.

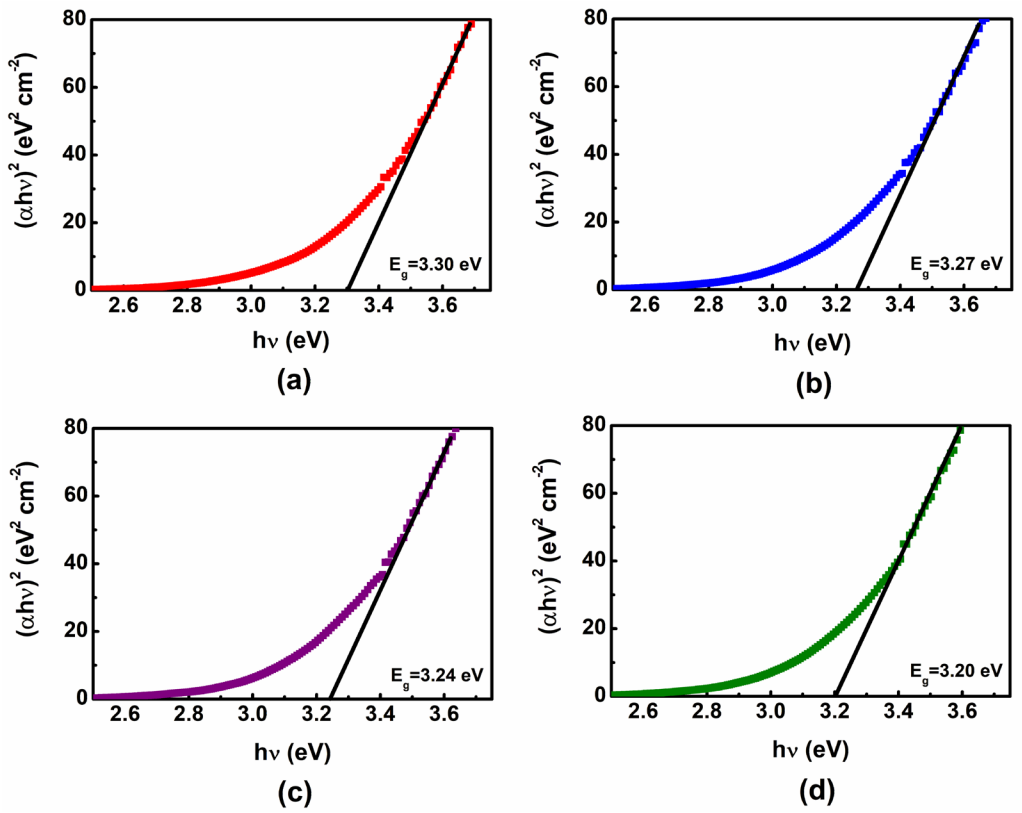


Figure 11. Tauc plots of (**a**) pure, (**b**) 2% Mn-doped, (**c**) (2% Mn, 1% Ce)co-doped, and (**d**) (2% Mn, 2% Ce)co-doped ZnS nanocrystals.

4.7. PL and Colorimetric Studies

A spectrofluorometer (FP-8300, JASCO Corporation, Tokyo, Japan; wavelength range: 200 nm–750 nm) was used to measure the PL spectra of water-dispersed materials. Figure 12 depicts the PL spectra of the pure, 2% Mn-doped, and (Mn, Ce)co-doped [(2% Mn, 1% Ce) and (2% Mn, 2% Ce)] ZnS nanocrystals. An excitation wavelength of 320 nm was used to record each of these spectra. The pure ZnS nanocrystals exhibit a broad emission in the range of 380–510 nm, which has been attributed to the presence of various intrinsic defects such as zinc interstitials, sulfur interstitials, sulfur vacancies, and zinc vacancies [11,74]. Mn doping significantly changes the PL properties of ZnS. Mn-doped ZnS exhibits strong yellow–orange emission with a peak at 580 nm. This emission is attributed to the $^4T_1$–$^6A_1$ transition of Mn^{2+} [66]. Incorporating Mn^{2+} ions alters the electron transition pathway from the CB, allowing transitions through the $^4T_1$ and $^6A_1$ levels of Mn^{2+} and resulting in yellow–orange emission. Furthermore, Mn doping quenches the broad emission in the 380–510 nm range. The lower PL intensity of (Mn, Ce)co-doped ZnS nanocrystals than that of Mn-doped ZnS nanocrystals may result from competing energy-transfer processes [75,76]. Incorporating Ce dopants introduces additional localized energy states within the band gap. Thus, these states can compete with energy transfer to Mn ions, reducing the radiative process. Furthermore, Ce ions have a significantly larger radius than Zn and Mn ions, and their incorporation can cause severe lattice strain and distortions, leading to deep-level traps. These defects act as non-radiative recombination centers, causing quenching of PL.

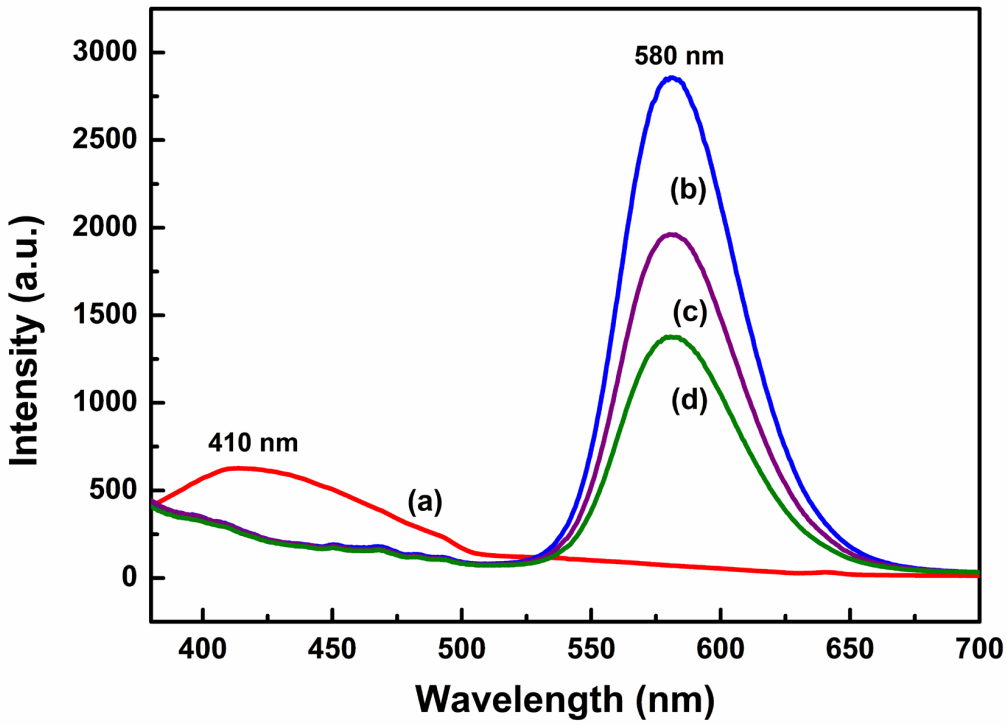


Figure 12. PL spectra of (a) pure, (b) 2% Mn-doped, (c) (2% Mn, 1% Ce)co-doped, and (d) (2% Mn, 2% Ce)co-doped ZnS nanocrystals.

The emission properties of the pure, Mn-doped, and (Mn, Ce)co-doped ZnS nanocrystals have been further illustrated using the CIE colorimetric system. The CIE diagram provides a standardized representation of human color perception [77]. Figure 13 presents the 1931 CIE diagrams for the pure, 2% Mn-doped, and (Mn, Ce)co-doped [(2% Mn, 1% Ce) and (2% Mn, 2% Ce)] ZnS nanocrystals. The colorimetric coordinates of the pure, 2% Mn-doped, (2% Mn, 1% Ce)co-doped, and (2% Mn, 2% Ce)co-doped ZnS nanocrystals are (0.191, 0.145), (0.495, 0.437), (0.483, 0.426), and (0.470, 0.414), respectively. The coordinates

change significantly after Mn doping. The coordinates also change with increasing Ce concentration. The CCT of each material has been found using the well-known McCamy's relation [78,79],

$$CCT = -449n^3 + 3525n^2 - 6823.3n + 5520.33 \quad (5)$$

where $n = (x - 0.3220)/(y - 0.1858)$. The CCTs of the pure, 2% Mn-doped, (2% Mn, 1% Ce)co-doped, and (2% Mn, 2% Ce)co-doped ZnS nanocrystals are 5090 K, 2347 K, 2395 K, and 2455 K, respectively. The colorimetric studies using CIE diagrams thus reveal that the emission properties of ZnS can be altered by Mn doping and (Mn, Ce) co-doping, signifying their enhanced application potential in optoelectronics.

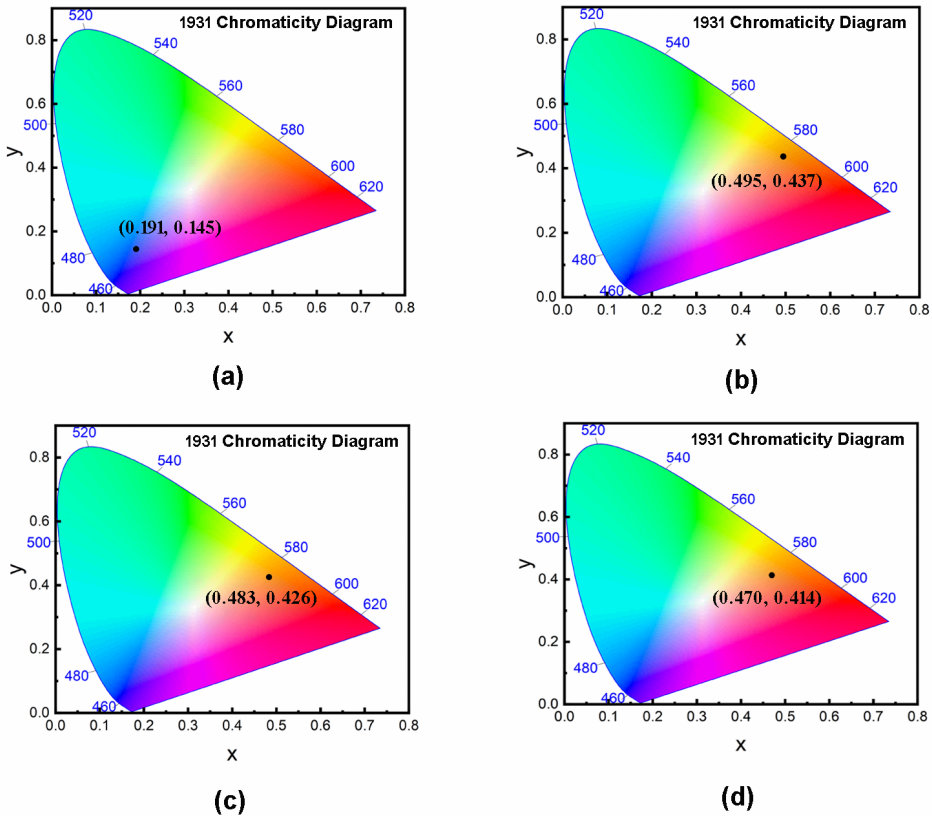


Figure 13. 1931 chromaticity diagrams of (**a**) pure, (**b**) 2% Mn-doped, (**c**) (2% Mn, 1% Ce)co-doped, and (**d**) (2% Mn, 2% Ce)co-doped ZnS nanocrystals.

4.8. Tetracycline Degradation Studies

The photocatalytic activities of the pure, 2% Mn-doped, and (Mn, Ce)co-doped [(2% Mn, 1% Ce) and (2% Mn, 2% Ce)] ZnS nanocrystals have been evaluated using tetracycline as an antibiotic pollutant. The experimental setup used for this purpose has been described earlier in the article. Initially, a stock aqueous solution was prepared by adding 0.02 g of tetracycline to 800 mL of deionized water, thereby obtaining a concentration of 25 mg L^{-1}. For each photocatalysis experiment, 60 mL of the tetracycline solution was transferred to the reactor's double-walled beaker, followed by the addition of 0.03 g of photocatalyst. The beaker was then kept in the dark for 60 min under mild magnetic stirring. After that, the lamp was switched on to initiate the photocatalysis process. A small quantity of solution was withdrawn from the reactor at certain time intervals and centrifuged to separate the photocatalyst from the solution. The absorption spectrum of the solution was recorded with a UV–visible spectrophotometer to monitor photodegradation.

The degradation efficiency (η) of each photocatalyst has been found using the following relation [80],

$$\eta = \frac{C_0 - C}{C_0} \times 100 = \frac{A_0 - A}{A_0} \times 100 \quad (6)$$

where C_0 and C are the tetracycline concentration before light exposure and the concentration of tetracycline after light exposure for a particular time, while A_0 and A are the absorbance before light exposure and the absorbance of tetracycline after light exposure for a particular time. The absorbance values corresponding to the absorption peak of tetracycline at 357 nm have been used to calculate the degradation efficiencies.

Figure 14 presents the absorption spectra of tetracycline treated with pure, 2% Mn-doped, (2% Mn, 1% Ce)co-doped, and (2% Mn, 2% Ce)co-doped ZnS nanocrystals as photocatalysts, after different hours of light irradiation. All cases show a gradual decrease in absorbance with increasing irradiation time, showing that the materials are effective in tetracycline photodegradation. The pure, 2% Mn-doped, (2% Mn, 1% Ce)co-doped, and (2% Mn, 2% Ce)co-doped ZnS nanocrystals showed degradation efficiencies of 45%, 64%, 89%, and 92% after 300 min of light irradiation, respectively. Thus, these results show that (Mn, Ce) co-doping can significantly enhance the photocatalytic efficiency of ZnS nanocrystals. Notably, the material with the best photocatalytic activity, i.e., (2% Mn, 2% Ce)co-doped ZnS, degraded a significant amount of tetracycline after 180 min (85%). The photodegradation behavior of each photocatalyst is illustrated by plotting C/C_0 versus irradiation time (Figure 15a). Furthermore, as shown in Figure 15b, the linear dependence of ln (C_0/C) on irradiation time shows that the degradation process for each of the photocatalysts follows pseudo-first-order kinetics according to the following equation [81],

$$\ln(C_0/C) = k_{app}\, t \quad (7)$$

where k_{app} is the apparent rate constant of photodegradation. The k_{app} values for pure, 2% Mn-doped, (2% Mn, 1% Ce)co-doped, and (2% Mn, 2% Ce)co-doped ZnS nanocrystals are 0.0020 min^{-1}, 0.0034 min^{-1}, 0.0076 min^{-1}, and 0.0090 min^{-1}, respectively. The (2% Mn, 2% Ce)co-doped ZnS exhibits the highest rate constant, showing its superior photocatalytic activity compared to other photocatalysts studied in this work.

Photocatalysis in a pure semiconductor occurs through various stages. First, the semiconductor absorbs light with energy equal to or greater than the band gap, exciting electrons from the VB to the CB and creating holes in the VB. Electrons and holes may move toward the surface or recombine. Electrons that reach the photocatalyst surface may react with O_2 to produce superoxide radicals. Again, those holes reaching the photocatalyst surface may react with OH^- ions, producing hydroxyl radicals. These highly reactive superoxide and hydroxyl radicals react with the pollutant, degrading it to H_2O, CO_2, etc. The various reactions that occur during photocatalysis are presented below [82,83].

$$ZnS + h\nu \rightarrow e^-(CB) + h^+(VB) \quad (8)$$

$$e^- + O_2 \rightarrow O_2^{*-} \quad (9)$$

$$h^+ + OH^- \longrightarrow OH^* \quad (10)$$

$$O_2^{*-} + \text{Tetracycline} \rightarrow \text{Degraded products} \quad (11)$$

$$OH^* + \text{Tetracycline} \rightarrow \text{Degraded products} \quad (12)$$

Intrinsic and extrinsic defects play important roles in enhancing the photocatalytic activity of semiconductors. These defects may introduce defect levels within the band gap. Electrons in the CB may transition to these levels, hindering electron-hole recombination, which is crucial for enhancing the photocatalytic activity of the material. The

considerable difference in ionic radii between Mn^{2+} (0.83 Å) and Ce^{4+} (0.93 Å), along with lattice strain-induced distortion, can generate internal electric fields due to altered electron-density distributions, enhancing electron-hole separation and increasing photocatalytic efficiency. Tuning charge distribution to generate internal electric fields that enhance electron-hole separation and improve photocatalysis has recently been reported for a few other photocatalysts [84–86].

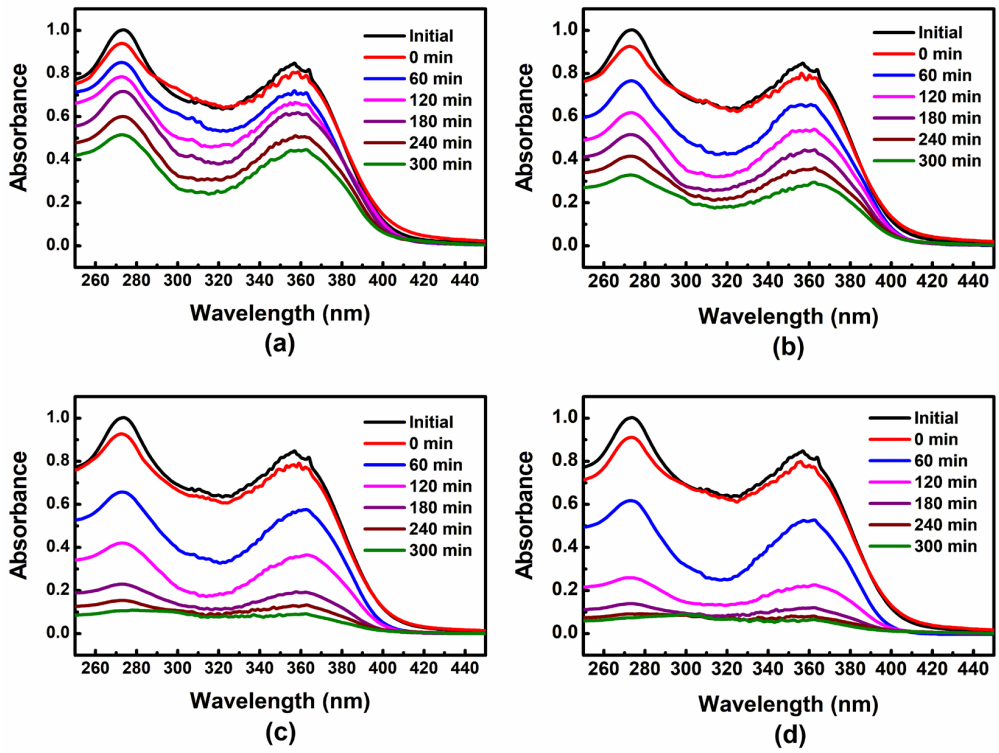


Figure 14. Absorption spectra of tetracycline with (**a**) pure, (**b**) 2% Mn-doped, (**c**) (2% Mn, 1% Ce)co-doped, and (**d**) (2% Mn, 2% Ce)co-doped ZnS nanocrystals as photocatalysts after different times of irradiation.

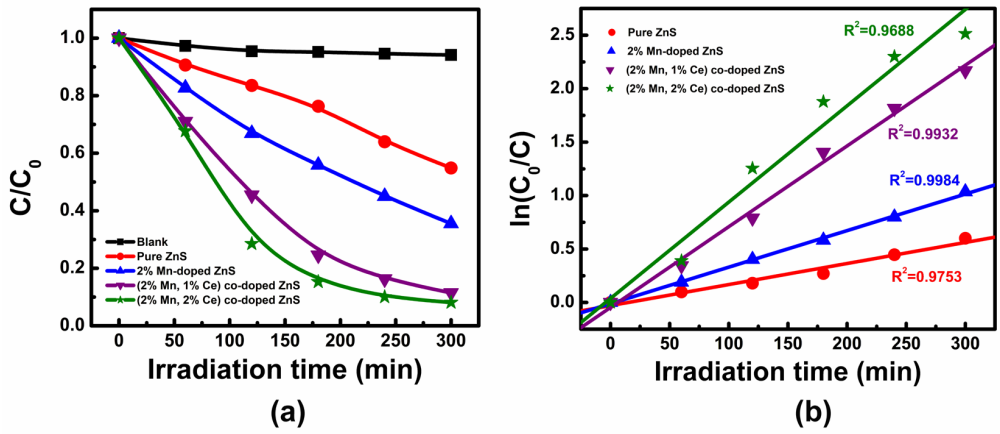


Figure 15. (**a**) C/C_0 versus irradiation time plots, and (**b**) ln (C_0/C) versus irradiation time plots.

Photocatalyst recyclability is an important parameter for assessing application viability, as it reduces precursor use, processing time, effort, and manufacturing costs. The photocatalyst with the best degradation efficiency, i.e., (2% Mn, 2% Ce)co-doped ZnS, has been used in recyclability tests over four cycles. After each cycle, the photocatalysts were separated from the solution using a centrifuge at 4000 rpm. The photocatalysts thus obtained were washed with deionized water and then used for the next cycle. Figure 16a presents the

degradation efficiencies after 300 min of light irradiation across 4 consecutive recyclability cycles. The degradation efficiency after 300 min of light exposure declined steadily from 92% to 85% across three recyclability tests, representing a 7.6% change from the 1st cycle. After four operational cycles, degradation efficiency decreased to 79%, a 14.1% change from the 1st cycle. The decrease in degradation efficiency may be due to material loss during processing and saturation of the photocatalyst after repeated operations. The XRD pattern of the (2% Mn, 2% Ce)co-doped ZnS nanocrystals collected after the 4th cycle was recorded and compared with the XRD pattern before the photodegradation process. The XRD patterns of the photocatalysts before and after photodegradation experiments are presented in Figure 16b. The results show an unchanged crystal structure, indicating the stability of the photocatalysts during photodegradation. The photocatalytic performance of (2% Mn, 2% Ce)co-doped ZnS was compared with a few recently reported photocatalysts (Table 1). The performance of the (2% Mn, 2% Ce)co-doped ZnS nanocrystals for tetracycline photodegradation was compared after 180 min of light exposure, during which significant degradation occurs. The comparison indicates promising prospects for (Mn, Ce)co-doped ZnS nanocrystals as a photocatalyst for tetracycline degradation.

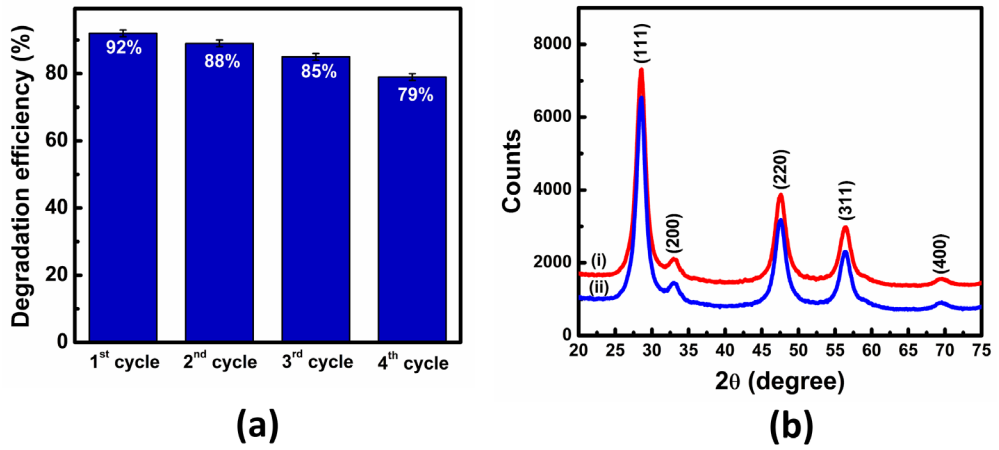


Figure 16. (**a**) Degradation efficiency of (2% Mn, 2% Ce)co-doped ZnS nanocrystals after 300 min of light irradiation for different cycles of operation and (**b**) XRD patterns of (2% Mn, 2% Ce)-co-doped ZnS nanocrystals (i) before photocatalysis and (ii) after the 4th cycle of photocatalytic operation.

Table 1. Tetracycline photodegradation efficiency of (Mn, Ce)co-doped ZnS compared with a few selected photocatalysts from the literature.

Photocatalyst	Tetracycline Concentration	Catalyst Loading	Light Source	Time	Degradation Efficiency (%)	Ref.
ZnOanchoredboron-doped graphitic carbon nitride	10 mgL^{-1}	20 mg	Visible light	180 min	76.7%	[82]
Mn-Sbco-doped SnO_2	20 mgL^{-1}	20 mg	Xe lamp	105 min	79.5%	[83]
ZnO/ZnS	20 mgL^{-1}	20 mg	Xe lamp	100 min	79%	[87]
$AgInS_2$/ZnS	40 mgL^{-1}	20 mg	Simulated sunlight	120 min	46%	[88]
$Zn_{0.6}Ba_{0.2}Cu_{0.2}Al_{0.7}Fe_{1.3}O_4$	10 mgL^{-1}	10 mg	Xe lamp	140 min	97.67%	[89]
ZnO-modified $Y_2Ti_2O_7$	15 mgL^{-1}	60 mg	UV light	180 min	76%	[90]
(2% Mn, 2% Ce) co-doped ZnS	25 mgL^{-1}	30 mg	Simulated sunlight	180 min	85%	This study

5. Conclusions

Pure, 2% Mn-doped, and (Mn, Ce)co-doped [(2% Mn, 1% Ce) and (2% Mn, 2% Ce)] ZnS nanocrystals were synthesized using the facile chemical co-precipitation method, and microstructural and optical properties have been systematically investigated. The pure ZnS nanocrystals exhibited a cubic crystal structure, which remained unaltered in the Mn-doped and (Mn, Ce)co-doped counterparts. However, the lattice parameter increased after Mn doping and (Mn, Ce) co-doping, which is attributed to the larger sizes of Mn and Ce ions than the Zn ion. A decrease in crystallite size, along with an increase in lattice strain and dislocation density, has been observed with Mn doping and (Mn, Ce) co-doping. The oxidation states of Mn ions and Ce ions in the (2% Mn, 2% Ce)co-doped ZnS nanocrystals were found to be +2 and +4, as revealed by XPS studies. The materials exhibit strong absorption in the UV region, with optical band gaps in the range of 3.20–3.30 eV. The Mn-doped and (Mn, Ce)co-doped ZnS nanocrystals exhibited a yellow–orange PL resulting from the $^4T_1$ to $^6A_1$ transition of Mn^{2+}. The emission properties of ZnS have been significantly altered by Mn doping and (Mn, Ce) co-doping, as revealed by PL and colorimetric studies, signifying their enhanced optoelectronic application potential. Quenching of the yellow–orange emission of Mn-doped ZnS was observed after Ce incorporation. The tetracycline photodegradation efficiencies of the pure, 2% Mn-doped, (2% Mn, 1% Ce)co-doped, and (2% Mn, 2% Ce)co-doped ZnS nanocrystals under simulated sunlight were 45%, 64%, 89%, and 92% after 300 min of light irradiation, respectively. Ce-induced increase in trap centers, the change in localized charge distribution with Ce doping, and the exhibition of a significantly different microstructure have been attributed to the superior photocatalytic activities of (Mn, Ce)co-doped ZnS compared with pure and Mn-doped ZnS. The recyclability of the (2% Mn, 2% Ce)co-doped ZnS nanocrystals for photocatalysis was investigated. The photocatalysts showed good recyclability over 3 cycles and photostability. This work provided significant insights into the effects of (Mn, Ce) co-doping on the structural, optical, and photocatalytic properties of ZnS nanocrystals. The (Mn, Ce)co-doped ZnS nanocrystals have been shown to be cost-effective, efficient, and recyclable photocatalysts for tetracycline degradation.

Author Contributions: Conceptualization, P.D. and M.P.C.K.; methodology, P.D. and M.P.C.K.; validation, P.D. and M.P.C.K.; formal analysis, P.D. and M.P.C.K.; investigation, P.D. and M.P.C.K.; resources, M.P.C.K.; data curation, P.D. and M.P.C.K.; writing—original draft preparation, P.D.; writing—review and editing, M.P.C.K.; visualization, P.D. and M.P.C.K.; supervision, M.P.C.K. All authors have read and agreed to the published version of the manuscript.

Funding: This research received no external funding.

Institutional Review Board Statement: Not applicable.

Informed Consent Statement: Not applicable.

Data Availability Statement: The data underlying this research will be made available by the corresponding author upon reasonable request.

Acknowledgments: The authors offer their sincere gratitude to SAIF, Gauhati University; CIF, Gauhati University; IASST, Guwahati; IIT, Delhi, and the Department of Chemistry, Cotton University for providing the XRD, FE-SEM, TEM, XPS, and FT-IR facilities, respectively.

Conflicts of Interest: The authors declare no conflicts of interest.

Abbreviations

The following abbreviations are used in this manuscript:

ZnS	Zinc sulphide
XRD	X-ray diffraction
TEM	Transmission electron microscope
FE-SEM	Field emission scanning electron microscope
EDX	Energy-dispersive X-ray
XPS	X-ray photoelectron spectrometer
FT-IR	Fourier transform infrared
PL	Photoluminescence
FWHM	Full width at half maximum
WH	Williamson–Hall
MWH	Modified Williamson–Hall
ICDD	International Centre for Diffraction Data
HR-TEM	High-resolution transmission electron microscope
ATR	Attenuated total reflectance
CIE	Commission Internationale de I'Eclairage
CCT	Correlated color temperature
VB	Valence band
CB	Conduction band

References

1. Azuma, T.; Tsukada, A.; Fujii, N.; Katagiri, M.; Nakamura, I.; Shimizu, H.; Tatsuno, K.; Watanabe, M.; Ohmagari, N.; Matsunaga, N. First Multi-Facility Antimicrobial Surveillance in Japanese Hospital Wastewater Reveals Spatiotemporal Trends and Source-Specific Environmental Loads. *Antibiotics* **2026**, *15*, 50. [CrossRef]
2. Sivalingam, P.; Ganapathy, D.; Poté, J. Livestock waste: A hidden source of extracellular clinically relevant high-risk antibiotic resistance genes in the environment. *Microbe* **2026**, *10*, 100664. [CrossRef]
3. Polak, D.; Kamocki, S.; Szwast, M. Evaluation of the Potential of Metal–Organic Compounds ZIF-8 and F300 in a Membrane Filtration–Adsorption Process for the Removal of Antibiotics from Water. *Antibiotics* **2025**, *14*, 619. [CrossRef]
4. Ali, M.M.; Zhang, L.; Xu, Y.; Gaballah, M.S.; Gaballah, E.S.; Samer, M.; Liu, Z. Nexus between anaerobic digestion of animal waste and antibiotic-related pollutants: A critical review. *Appl. Energy* **2025**, *382*, 125284. [CrossRef]
5. Cai, S.; Ma, C.; Srinivasakannan, C.; Xue, G.; Wang, L.; Wang, Y.; Duan, X. Tetracycline-derived N/P co-doped porous graphene-like carbon for effective removal of tetracycline: Synergistic adsorption-degradation mechanism. *J. Environ. Chem. Eng.* **2026**, *14*, 121174. [CrossRef]
6. Rana, M.S.; Putul, R.A.; Salsabil, N.; Kabir, M.T.; Hossain, M.S.; Masum, S.M.; Molla, M.A.I. Solar-Driven Photodegradation of Methylene Blue Dye Using Al-Doped ZnO Nanoparticles. *Appl. Nano* **2026**, *7*, 3. [CrossRef]
7. Zhang, M.; Liu, H. Silsesquioxane-Based Hybrid Semiconductor Polymers for Efficient Antibiotic Photodegradation and Detection Simultaneously. *ACS Appl. Polym. Mater.* **2025**, *7*, 4633–4643. [CrossRef]
8. Liu, J.; Ruan, H.; Duan, P.; Shao, P.; Zhou, Y.; Wang, Y.; Chen, Y.; Yan, Z.; Liu, Y. Photocatalytic Degradation of Antibiotics Using Nanomaterials: Mechanisms, Applications, and Future Perspective. *Nanomaterials* **2026**, *16*, 49. [CrossRef]
9. Mishra, S.; Rajaboina, R.K.; Jho, Y.-D. Review on the Hierarchical Improvement of Zinc Sulfide-Based Nanogenerator Systems and Their Various IoT Applications. *ACS Appl. Energy Mater.* **2025**, *8*, 1918–1941. [CrossRef]
10. Tiwari, A.; Bishnoi, S.; Dhoble, S.J. Engineering ZnS nanoarchitectures: Defects and dynamic surfaces for improved photocatalysis. *J. Mol. Struct.* **2026**, *1349*, 143750. [CrossRef]
11. Vikkash, R.; Muthukumaran, S.; Rakchana, M. Structural, photoluminescence, and photo-catalytic analysis of Mn and Cr dual doped ZnS nanostructures via co-precipitation route. *J. Phys. Chem. Sol.* **2025**, *207*, 112892. [CrossRef]
12. Dile, M.; Laganovska, K.; Vanags, E.; Ignatans, R.; Vitola, V.; Zolotarjovs, A.; Leimane, M.; Einbergs, E.; Smits, K. Evolution of ZnS:Cu nanoparticle morphology during microwave-assisted hydrothermal synthesis. *Nano Struct. Nano-Obj.* **2025**, *41*, 101450. [CrossRef]
13. Liu, B.; Li, X.; Zhang, L.; Ma, C.; Chen, Y.; Wang, X.; Wei, H.; Wang, P. In Situ Crystalline Growth ZnS Nanoparticles on Conjugated Polymer for Enhancement of the Photocatalytic Performance. *Polymers* **2025**, *17*, 575. [CrossRef]
14. Arsad, A.Z.; Zuhdi, A.W.M.; Abdullah, S.F. Impact of annealing temperatures on the physical properties of zinc sulfide thin films prepared by sol-gel spin coating method. *Ceram. Int.* **2025**, *51*, 31270–31285. [CrossRef]
15. Verduzco, A.C.; Aguilar, J.U.B.; Huitrón, J.C.A. Photoluminescence and electroluminescence properties of Cu-doped ZnS thin films fabricated by ultrasonic spray pyrolysis. *J. Alloys Compd.* **2025**, *1022*, 179834. [CrossRef]

16. Feng, C.; Zhang, H.; Deng, Y.; An, Y.; Chen, X.; Sun, J.; Zhang, M.; Dong, L. High wurtzite content ZnS:Mn with better luminescent performances prepared at lower temperature by a ball milling method. *J. Alloys Compd.* **2023**, *968*, 172211. [CrossRef]
17. Xu, W.; Chen, K.; Wang, X.; Zhao, X.; Xu, M.; Chen, W.; Pan, X. Defective ZnS yolk-shell nanospheres with sulfur vacancy for efficient sonocatalytic H_2 production. *Mater. Lett.* **2025**, *381*, 137749. [CrossRef]
18. Mukhina, M.V.; Butterfield, A.G.; Young, H.L.; McCormick, C.R.; Schaak, R.E.; Kleckner, N. Faulted ZnS:Mn,Cu Nanorods Provide Nanoscale Mechanoluminescence Excitation in Biologically Relevant Force Range. *ACS Nano* **2026**, *20*, 9348–9357. [CrossRef]
19. Samanta, D. Glucose mediated biosynthesis of pristine ZnS and Ag-ZnS nanostructures for waste-water treatment: The antagonistic effect between ZnS and Ag. *J. Cryst. Growth* **2025**, *668*, 128294. [CrossRef]
20. Mishra, S.; Supraja, P.; Sankar, P.R.; Kumar, R.R.; Prakash, K.; Haranath, D. Controlled synthesis of luminescent ZnS nanosheets with high piezoelectric performance for designing mechanical energy harvesting device. *Mater. Chem. Phys.* **2022**, *277*, 125264. [CrossRef]
21. Zhang, J.; Qi, K.; Pitcheri, R.; Duan, C. Engineering ZnS quantum dots for photocatalysis: Synthesis, modifications, and multifunctional applications. *J. Photochem. Photobio. C Photochem. Rev.* **2025**, *65*, 100722. [CrossRef]
22. Patel, P.C.; Ghosh, S.; Upadhyay, A.N. Carrier-mediated ferromagnetism vs antiferromagnetic compensation in co-doped ZnS nanoparticles. *J. Phys. Chem. Sol.* **2026**, *210*, 113373. [CrossRef]
23. Gün, B.Ş.; Aydoğan, A.; Çadırcı, M.; Şensoy, S.; Gurbanov, R.; Tunalı, B. Green synthesis of quercetin-mediated ZnS quantum dots and their photocatalytic, antimicrobial, and cytotoxic performances. *Sci. Rep.* **2025**, *15*, 45236. [CrossRef]
24. Saleem, S.; Khalid, S.; Malik, M.A.; Nazir, A. Review and Outlook of Zinc Sulfide Nanostructures for Supercapacitors. *Energy Fuels* **2024**, *38*, 9153–9185. [CrossRef]
25. Talbi, A.; Khaaissa, Y.; Mansouri, F.; El Khouja, O.; Chaouiki, A.; Nouneh, K.; AlObaid, A.A. Advancing Solar Cell Efficiency: Experimental and Numerical Analysis of Mn-doped ZnS as a Buffer Layer. *ACS Omega* **2025**, *10*, 28220–28232. [CrossRef]
26. Göktaş, A.; Yesilçimen, M.; Kilic, A.; Göktaş, S.; Tumbul, A. Synergistic Co–Cu dual doping in ZnS thin Films: Unlocking high room-temperature ferromagnetism and UV-activated photocatalytic efficiency for multifunctional applications. *Mater. Chem. Phys.* **2025**, *346*, 131399. [CrossRef]
27. Khan, J.; Wei, Y.; Khan, Y.; Younis, M.Y. Bimetallic Cu-Bi Co-Doped ZnS Nanostructures: Enhanced Optical and Electrochemical Properties for photocatalytic degradation of organic pollutants. *J. Mol. Struct.* **2025**, *1344*, 142950. [CrossRef]
28. Murugan, S.; Ashokkumar, M. Enhanced sunlight-driven photocatalytic activity of (Cu, TM) (TM = Mg, Mn, Ag) dual-doped ZnS quantum dots for multi-dye degradation and improved reusability through PVA polymer Integration. *Mater. Sci. Eng. B* **2025**, *316*, 118139. [CrossRef]
29. Chandrika, R.H.; Mary, S.S.; Pavithraa, A.R.; Jothivenkatachalam, K.; Ramar, M. Effect of Cu and Fe Co-doped ZnS nanoparticles for the efficient antibacterial and photocatalytic applications. *Inorg. Chem. Commun.* **2026**, *186*, 116097. [CrossRef]
30. Vikkash, R.; Muthukumaran, S.; Rakchana, M. Enhanced photoluminescence and photocatalytic performance of Mn and Co simultaneously doped ZnS nanostructures by co-precipitation method. *J. Mater. Sci. Mater. Electron.* **2025**, *36*, 1483. [CrossRef]
31. Chen, X.; Ge, W.; Wang, Y.; Li, J. ZnS:Er^{3+}/Yb^{3+} phosphor for optical temperature sensing and dual-mode anti-counterfeiting. *J. Alloys Compd.* **2023**, *966*, 171651. [CrossRef]
32. Peng, Y.; Zhang, F.; Zhang, Y.; Luo, X.; Chen, L.; Shi, Y. ZnS modified N, S dual-doped interconnected porous carbon derived from dye sludge waste as high-efficient ORR/OER catalyst for rechargeable zinc-air battery. *J. Colloid Interface Sci.* **2022**, *616*, 659–667. [CrossRef]
33. Bailón-Ruiz, S.J.; Cedeño-Mattei, Y.; Colón-Dávila, N.; Alamo-Nole, L. Enhanced Antibiotic Removal Using Fe-Doped ZnS Nanoparticles. *Micro* **2026**, *6*, 25. [CrossRef]
34. Raza, A.; Zahra, S.T.; Noor, H.; Naseem, S.; Riaz, S.; Khan, M.E.; Ali, W.; Alomar, M.S.; Khan, A.U.; Ali, S.K.; et al. Excellent Photocatalytic Performance Against Amoxicillin Antibiotic and Pt-Free Hydrogen Production Using Fe-Doped ZnS Nanostructures: Reaction Kinetics and Mechanistic Insights. *Catalysts* **2025**, *15*, 165. [CrossRef]
35. Sonkar, R.; Mondal, N.J.; Thakur, S.; Saikia, E.; Ghosh, M.P.; Chowdhury, D. Cobalt-substituted ZnS QDs: A diluted magnetic semiconductor and efficient photocatalyst. *Nanoscale Adv.* **2023**, *5*, 7042–7056. [CrossRef]
36. Malik, A.Q.; Jabeen, T.; Khan, A.; Ansari, M.A.; Kumar, A. Ginger-derived polymer modified with Mn-doped zinc sulphide quantum dots as photocatalyst for pharmaceutical pollutants elimination with DFT studies. *J. Mol. Liq.* **2025**, *419*, 126766. [CrossRef]
37. Li, S. Hydrothermal synthesis of Cu-doped ZnS for enhanced photocatalytic degradation of tetracycline under visible light. *IOP Conf. Ser. Earth Environ. Sci.* **2021**, *769*, 022053. [CrossRef]
38. Das, P.; Talukdar, H.; Kalita, M.P.C. Protein-assisted synthesis of Mn-doped ZnS nanocrystals and evaluation of their capabilities for anti-counterfeiting and photodegradation of antibiotic pollutants. *MRS Adv.* **2026**, *11*, 1472–1479. [CrossRef]
39. Ibrahim, S.; Ghosh, S.; Pal, T. Synthesis and characterization of solution-processable $Cd_{1-x}Zn_xS$ nanorods for photocatalytic degradation of tetracycline. *J. Mater. Sci. Mater. Electron.* **2020**, *31*, 12955–12960. [CrossRef]

40. Diego-Rucabado, A.; Merino-Garcia, I.; Espeso, J.I.; González, J.; Arce, B.; Valiente, R.; Beobide, G.; Cano, I.; Martín-Rodríguez, R.; de Pedro, I.; et al. Visible Light Active Ce-Doped and Cu–Ce co-doped TiO_2 Nanocrystals and Optofluidics for Clean Alcohol Production from CO_2. *ACS Sustain. Chem. Eng.* **2023**, *11*, 13260–13273. [CrossRef]
41. Islam, R.; Abdur, R.; Alam, M.A.; Munna, N.; Ahmed, A.N.; Hossain, M.; Bashar, M.S.; Islam, D.; Jamal, M.S. Modulating Mn-doped NiO nanoparticles: Structural, optical, and electrical property tailoring for enhanced hole transport layers. *Nanoscale Adv.* **2025**, *7*, 133–143. [CrossRef]
42. Sakthivel, P.; Mangalaraja, R.V.; Ramalingam, G.; Sakthipandi, K.; Gowtham, V. Synthesis, Structure, Morphology, Element composition, Electrochemical, and Optical studies of $Zn_{0.98-X}Mn_{0.02}Ce_X$ Quantum dots. *Spectrochim. Acta A* **2023**, *303*, 123140. [CrossRef]
43. Yang, S.-H.; Lial, Y.-J.; Cheng, N.-J.; Ling, Y.-H. Preparation and characteristics of yellow ZnS:Mn,Ce phosphor. *J. Alloys Compd.* **2010**, *489*, 689–693. [CrossRef]
44. Sun, X.; Yang, H.; Xie, J.; Teng, G.; He, J.; Zhao, Z.; Zhang, C. A photocatalyst combined of copper doped ZnO and graphdiyne (Cu/ZnO@GDY) for photocatalytic degradation of tetracycline: Mechanism and application. *Water Res.* **2025**, *278*, 123345. [CrossRef]
45. Ma, J.; Chen, Y.; Zhou, G.; Ge, H.; Liu, H. Recent Advances in Photocatalytic Degradation of Tetracycline Antibiotics. *Catalysts* **2024**, *14*, 762. [CrossRef]
46. Klug, H.P.; Alexander, L.E. *X-ray Diffraction Procedures for Polycrystalline and Amorphous Materials*, 2nd ed.; Wiley: New York, NY, USA, 1974; p. 635.
47. Williamson, G.K.; Hall, W.H. X-ray line broadening from filed aluminium and wolfram. *Acta Metall.* **1953**, *1*, 22–31. [CrossRef]
48. Zak, A.K.; Majid, W.H.A.; Abrishami, M.E.; Yousefi, R. X-ray analysis of ZnO nanoparticles by Williamson–Hall and size–strain plot methods. *Solid State Sci.* **2011**, *13*, 251–256. [CrossRef]
49. Ungár, T.; Tichy, G. The Effect of Dislocation Contrast on X-Ray Line Profiles in Untextured Polycrystals. *Phys. Status Solidi A* **1999**, *171*, 425–434. [CrossRef]
50. Révész, Á.; Ungár, T.; Borbély, A.; Lendvai, J. Dislocations and grain size in ball-milled iron powder. *Nanostruct. Mater.* **1996**, *7*, 779–788. [CrossRef]
51. Kysar, J.W.; Gan, Y.X.; Morse, T.L.; Chen, X.; Jones, M.E. High strain gradient plasticity associated with wedge indentation into face-centered cubic single crystals: Geometrically necessary dislocation densities. *J. Mech. Phys. Solids* **2007**, *55*, 1554–1573. [CrossRef]
52. Deka, K.; Kalita, M.P.C. Microstructural Properties of Chemically Synthesized Cubic ZnS Nanocrystals. *Braz. J. Phys.* **2015**, *45*, 36–40. [CrossRef]
53. Mamiyev, Z.Q.; Balayeva, N.O. Optical and structural studies of ZnS nanoparticles synthesized via chemical in situ technique. *Chem. Phys. Lett.* **2016**, *646*, 69–74. Erratum in *Chem. Phys. Lett.* **2016**, *662*, 333. [CrossRef]
54. Qaisar, M.A.F.; Ali, S.; Ullah, I.; Parkash, A.; Malik, S.A.; Irfan, A.; Ali, S.; Qi, J.; Han, W. Superior Diffusion Kinetics of Zn^{2+} Over Monovalent Ions in MoS_2 Nanosheets for High-Power Supercapacitive Energy Storage. *Adv. Sustain. Syst.* **2026**, *10*, e01649. [CrossRef]
55. Basta, A.H.; Lotfy, V.F. Optimizing the lignin nanoparticles from different pulping by-products in developing cotton-based nanocrystalline cellulose for UV-light blocking. *Sci. Rep.* **2025**, *15*, 27165. [CrossRef]
56. Darwish, S.M.; Darwish, I.M. Spectroscopic investigation of tau protein conformational changes by static magnetic field exposure. *J. Phys. Commun.* **2022**, *6*, 075004. [CrossRef]
57. Li, Z.; Wang, Y.; Kozbial, A.; Shenoy, G.; Zhou, F.; McGinley, R.; Ireland, P.; Morganstein, B.; Kunkel, A.; Surwade, S.P.; et al. Effect of airborne contaminants on the wettability of supported graphene and graphite. *Nat. Mater.* **2013**, *12*, 925–931. [CrossRef]
58. Mtar, S.; Shova, S.; Boujelbene, M. Amorphous benzylammonium hydrogen sulfate hydrate: Structural disorder and optical properties of a new hybrid form. *J. Mol. Struct.* **2026**, *1361*, 145620. [CrossRef]
59. Dengo, N.; Vittadini, A.; Natile, M.M.; Gross, S. In-Depth Study of ZnS Nanoparticle Surface Properties with a Combined Experimental and Theoretical Approach. *J. Phys. Chem. C* **2020**, *124*, 7777–7789. [CrossRef]
60. Ali, A.H.; Hashem, H.A.; Elfalaky, A. Preparation, Properties, and Characterization of ZnS Nanoparticles. *Eng. Proc.* **2023**, *31*, 74. [CrossRef]
61. Shekhawat, A.; Kahu, S.; Saravanan, D.; Jugade, R. Synergistic behaviour of ionic liquid impregnated sulphate-crosslinked chitosan towards adsorption of Cr (VI). *Int. J. Bio. Macromol.* **2015**, *80*, 615–626. [CrossRef]
62. Varughese, G. Characterization and Optical Study on Zinc Sulphide Nanostructures doped with Gadolinium ions. *Mater. Today Proc.* **2016**, *3*, 282–288. [CrossRef]
63. Elsi, S.; Mohanapriya, S.; Pushpanathan, K. Observation of Novel Superparamagnetism in ZnS:Co Quantum Dots. *J. Supercond. Nov. Magn.* **2020**, *33*, 3223–3240. [CrossRef]

64. Wu, X.; Wan, T.L.; Yang, B.; Kuo, D.-H.; Zhang, P.; Liu, M.; Adawara, S.N.; Lu, D.; Lin, J.; Chen, X. A Mo-cation/O-anion doping strategy for creating vacancy defects and cation multivalency to enhance the hydrogen evolution of ZnS under visible light. *J. Mater. Chem. A* **2025**, *13*, 17976. [CrossRef]
65. Goudar, J.A.; Chapi, S.; Attar, M.; Thrinethra, S.N.; Vijeth, H.; Murugendrappa, M.V. Structural tuning, electrical conductivity, and electrochemical performance of in-situ polymerized PPy/Co-Doped Ni–Mn ferrites. *J. Solid State Electrochem.* **2026**. [CrossRef]
66. Bhargava, R.N.; Gallagher, D.; Hong, X.; Nurmikko, A. Optical Properties of Manganese-Doped Nanocrystals of ZnS. *Phys. Rev. Lett.* **1994**, *72*, 416–419. [CrossRef]
67. Wang, H.; Zhao, M.; Zhao, F.; Shang, W.; Li, H.; Zhao, R.; Guo, P.; Bao, J. Efficient Ce–Ti/coal gangue catalysts *via* microwave synthesis for NH_3-SCR: Enhanced activity and mechanistic insights. *Nanoscale* **2026**, *18*, 7583.
68. Idriss, H. Study of reduced states of $Ce_{1-y}Fe_yO_2$ and $Ce_{1-y}U_yO_2$ for the thermochemical water splitting to hydrogen. *Sustain. Energy Fuels* **2026**, *10*, 2440–2460. [CrossRef]
69. Murugadoss, G.; Venkatesh, N.; Venkatesan, R.; Kim, S.-C.; Gnanasekaran, L.; Moovendhan, M. Synergistic enhancement of the photocatalytic and antibacterial activities of cerium and tin-doped zinc sulfide nanoparticles. *Surf. Interfaces* **2026**, *86*, 108798. [CrossRef]
70. Suganthi, N.; Puspanathan, K. Effect of phase transition on room temperature ferromagnetism in cerium doped ZnS nanorods. *Trans. Nonferrous Met. Soc. China* **2019**, *29*, 811–820. [CrossRef]
71. Tauc, J. Absorption edge and internal electric fields in amorphous semiconductors. *Mater. Res. Bull.* **1970**, *5*, 721–730. [CrossRef]
72. Han, L.; Cao, Y.; Chen, Y.; Tian, L.; Tian, W.; Li, Z. Enhanced Luminescence Properties of ZnS Nanoparticles for LEDs applications via Doping and Phase Control. *ACS Appl. Nano Mater.* **2025**, *8*, 8445–8454. [CrossRef]
73. Yang, X.; Gu, W.; Yuan, C.; Yang, Z.; Shi, S.; Liu, Z.; Liang, S.; Teng, F. A straightforward one-pot approach to two new defect energy levels in ZnS. *Cryst. Eng. Commun.* **2021**, *23*, 1999. [CrossRef]
74. Hernández-Hernández, L.A.; Pescador-Rojas, J.A.; Santana-Rodríguez, G.; Martínez-Farías, F.J.; Rangel-Cortes, E.; Meléndez-Lira, M.; Hernández-Hernández, A.; Rubio-Ponce, A. Interplay of luminescence and magnetic phenomena in Mn-doped ZnS zinc blende nanocrystals: Influence of magnetic doping. *J. Lumin.* **2025**, *277*, 120870. [CrossRef]
75. Balayeva, N.O.; Mamiyev, Z.Q. Synthesis and studies of CdS and ZnS-PE/NBR modified thermoplastic elastomeric copolymer nanocomposite films. *Mater. Lett.* **2016**, *162*, 121–125. [CrossRef]
76. Ayub, A.; Rauf, A.; Anam, A.; Alshammari, R.H.; Azam, M.Z.; Ambreen, N.; Arshad, M. Structural and optical advances in Cu/Sr Co-doped ZnO nanomaterials for accelerated photocatalytic degradation of organic pollutant. *RSC Adv.* **2026**, *16*, 13896–13913. [CrossRef]
77. Ruivo, A.; Laia, C. CIE color coordinates for the design of luminescent glass materials. *Color Res. Appl.* **2024**, *49*, 199–214. [CrossRef]
78. Pu, Y.; Guo, H.; Xie, J.; Wu, D.; Liu, H. Luminescence performance of borate glass co-doped with Tb^{3+}-Eu^{3+}. *Phys. B* **2026**, *739*, 418917. [CrossRef]
79. Perumal, R.N.; Lopez, A.X.; Subalakshmi, G. Synthesis and multi-colour luminescence spectra of RE^{3+} (RE^{3+} = Eu^{3+}, Sm^{3+}, Dy^{3+}, Eu^{3+}/Sm^{3+}/Dy^{3+}) doped $BiLa_2O_4$ phosphors. *Optik* **2018**, *170*, 125–131. [CrossRef]
80. Chen, J.; Xiong, Y.; Duan, M.; Li, X.; Li, J.; Fang, S.; Qin, S.; Zhang, R. Insight into the Synergistic Effect of Adsorption-Photocatalysis for the Removal of Organic Dye Pollutants by Cr-Doped ZnO. *Langmuir* **2020**, *36*, 520–533. [CrossRef]
81. Chiu, Y.-H.; Chang, T.-F.M.; Chen, C.-Y.; Sone, M.; Hsu, Y.-J. Mechanistic Insights into Photodegradation of Organic Dyes Using Heterostructure Photocatalysts. *Catalysts* **2019**, *9*, 430. [CrossRef]
82. Vu, N.H.; Huong, L.M.; Dat, N.M.; Nam, N.T.H.; Hieu, N.H. ZnO anchored boron-doped graphitic carbon nitride as a visible light responsive photocatalyst for enhancing tetracycline degradation and cytotoxicity studies. *J. Mater. Sci.* **2026**, *61*, 3793–3819. [CrossRef]
83. Mushtaq, R.; Ahmad, T.; Wani, F.; Kamili, K.; Bhat, S.A.; Nazeer, A.; haq, M.-u.; Ansari, M.Z. Mn–Sb Co-doped SnO_2 nanoparticles as efficient photocatalysts for tetracycline degradation. *RSC Adv.* **2026**, *16*, 17801–17814. [CrossRef]
84. Liu, Y.; Jiang, J.; Li, T.; Li, J.; Sun, T.; Liu, H.; Zhao, C.; Yan, G.; Li, M.; Huo, M.; et al. Tuning charge distribution for synergistic enhancement of internal electric field in BiOCl via phosphorus-vanadium dual-doping. *Appl. Catal. B* **2025**, *365*, 124964. [CrossRef]
85. Yuan, X.; Huang, W.; Xiang, S.; Yang, C.; Ding, K.; Zhang, J.; Hou, Y. Synergistic Cu and O co-doping in crystalline carbon nitride for enhanced photocatalytic degradation of organic pollutants via peroxymonosulfate activation. *Appl. Surf. Sci.* **2026**, *731*, 66433. [CrossRef]
86. Liu, X.; Chao, J.; Guo, F.; Chang, L.; Zhang, X.; Long, W.; Xi, Z. Gd and Zr Co-Doped $BiFeO_3$ Magnetic Nanoparticles for Piezo-Photocatalytic Degradation of Ofloxacin. *Nanomaterials* **2025**, *15*, 792. [CrossRef]
87. Feng, M.; Wei, Y.; Zhang, Y.; Xu, J.; Xu, J.; Yang, Z.; Qi, J.; Li, D.; You, F. Hollow structured ZnS/ZnO heterojunction for efficient tetracycline photodegradation. *Surf. Interfaces* **2026**, *89*, 109137. [CrossRef]

88. Dong, S.; Yang, Y.; Zada, A.; Liu, S.; Qi, K. Performance and mechanism of photocatalytic tetracycline degradation by $AgInS_2/ZnS$ composites. *J. Water Proc. Eng.* **2025**, *73*, 107695. [CrossRef]
89. Celik, C.; Yasar, M.; Alzahrani, K.J.; Abbas, M.; Ganesan, S.; Mujtaba, A.; Mishra, S.; Sharma, J.; Sinha, A.; Alzahrani, F.M. Synthesis, characterization, and mechanistic insights into enhanced photocatalytic tetracycline degradation by zinc-doped ferrite nanoparticles. *J. Sol. Gel. Sci. Technol.* **2026**, *117*, 71. [CrossRef]
90. Arfoy, B.; Khaddoudi, I.; Loubbidi, L.; Elmourabit, M.; El Haddade, O.; Allaoui, I.; El Hachmi, A.; Douma, M.; Chtoun, E.H. Photocatalytic degradation of tetracycline using ZnO-modified $Y_2Ti_2O_7$ nanoparticles. *Micro Nanostruct.* **2026**, *210*, 208508. [CrossRef]

Disclaimer/Publisher's Note: The statements, opinions and data contained in all publications are solely those of the individual author(s) and contributor(s) and not of MDPI and/or the editor(s). MDPI and/or the editor(s) disclaim responsibility for any injury to people or property resulting from any ideas, methods, instructions or products referred to in the content.